Monitoring Glacier Changes using Multitemporal Multipolarization SAR Images

Vahid Akbari, *Student Member, IEEE*, Anthony P. Doulgeris, *Member, IEEE*, and Torbjørn Eltoft, *Member, IEEE*

***Abstract*—This paper presents a processing chain for change detection of Arctic glaciers from multitemporal multipolarization synthetic aperture radar images. We produce terrain corrected multilook complex (MLC) covariance data by including the effects of topography on both geolocation and SAR radiometry as well as azimuth slope variations on polarization signature. An unsupervised contextual non-Gaussian clustering algorithm is employed for segmentation of each terrain corrected polarimetric SAR image and subsequently labeled with the aid of ground truth data into glacier facies. We demonstrate the consistency of the segmentation algorithm by characterizing the expected random error level for different SAR acquisition conditions. This allows us to determine whether an observed variation is statistically significant and therefore can be used for post-classification change detection of Arctic glaciers. Subsequently, the average classified images of succeeding years are compared, and changes are identified as the detected differences in the location of boundaries between glacier facies. In the current analysis, a series of dual polarization C-band ENVISAT ASAR images over the Kongsvegen glacier, Svalbard, is used for demonstration.**

***Index Terms*—Polarimetric synthetic aperture radar (PolSAR); radiometric terrain correction; matrix log-cumulant diagram; multilook product model; unsupervised contextual non-Gaussian segmentation; post-classification change detection.**

I. Introduction

CHANGES in the Arctic glaciers and ice caps provide a visible manifestation of climate change. Being recognized as potentially the largest short term contributors to sea level rise and having been observed to be one of the fastest warming areas on the planet [1], the present state of the Arctic ice masses, and changes over time, are of scientific and social importance.

As the climate changes, so too do the variables affecting glaciers. Identifying and monitoring fluctuations in glacier facies provide a means to track climate change. The only feasible method to obtain good spatial and temporal coverage of the Arctic glaciers is through the use of satellites. Spaceborne synthetic aperture radar (SAR) instruments, operating independently of weather and daylight, are a particularly valuable tool in Arctic areas. SAR has an added advantage over higher frequency instruments (visible and laser) because the signal penetrates some distance into the glacier such that the return signal is influenced not only by the surface, but also by the shallow subsurface. Another advantage of SAR in glacier monitoring is its sensitivity to moisture content and surface roughness, which enables it to detect different glacial zones. The multipolarization SAR may provide the additional information, and thus is a better tool for glacier monitoring than single polarization SAR sensors.

The authors are with the Department of Physics and Technology, University of Tromsø, 9037 Tromsø, Norway (e-mail:vahid.akbari@uit.no; anthony.p.doulgeris@uit.no; torbjorn.eltoft@uit.no)

It is appreciated that a difference in radar backscattering between multitemporal multipolarization SAR data may be caused by several factors such as actual land cover change, differerences in viewing geometry, surface topography, differerences in polarization configuration, and differerences in meteorological conditions. These considerations motivate us to develope a processing chain for glacier change detection which consists of five major steps: 1) multilooking, 2) terrain correction, 3) probability density function (PDF) selection, 4) unsupervised segmentation, and 5) post-classification change detection. Models accounting for temporal variation in multitemporal multipolarization SAR images should separate useful temporal variation, i.e., land cover or seasonal changes from variation arising due to other factors mentioned above.

Spaceborne SAR instruments have proven to be a very useful tool for multitemporal image analysis. However, terrain topography has significant impact on the geometric and radiometric quality of SAR images. For the geometric correction of topographic effect, precise terrain geocoding of SAR data is required. This can be accomplished by using a digital elevation model (DEM) and precise satellite state vector. In addition to geometric distortions, surface slopes modulates SAR backscatter which can be split into two main effects. The first effect is changes in radar cross sections (RCS) per unit image area [2], [3] and the second effect is that polarization states are also affected since the terrain slopes specially azimuthal slopes induce polarization orientation changes [4], [5]. Hence, before analyzing the data, terrain correction is a prerequisite for intercomparisions of multitemporal SAR images. This paper therefore addresses the precise geocoding and geometric terrain correction (GTC) of SAR data and then radiometric terrain correction (RTC) of multipolarization SAR data that utilizes the pixel size normalization on each element of the sample covariance matrix [6]. Moreover, orientation angle compensation (OAC) is included immediately following after the RTC [7]. Accurate backscatter estimates enable more robust use of the retrieved values for our task of change detection, as well as other applications such as land cover classification, monitoring of changes, edge detection and retrieval of geophysical parameters.

The scaled Wishart distribution, denoted $s\mathcal{W}_d^{\mathbb{C}}$, is the simplest PDF to model multilooked polarimetric SAR data in *homogeneous* areas. Non-Gaussian probability distributions provide better representation of the data for areas with pronounced heterogeneity, or high texture. Such distributions can be obtained using a matrix version of the

product model. The product model describes the covariance matrix as the product of a positive scalar texture component and a Wishart matrix speckle component [8], [9]. Several statistical models have been proposed in the literature to describe the texture term. For *textured* areas, the $\mathcal{K}_d$ model is commonly used (e.g., [10]). However, the analysis shows that this model does not always represent the data well. The $\mathcal{G}_d^0$-distribution is another multivariate distribution [11] to model *extremely heterogeneous* data. The two parameter Kummer-U distribution has been introduced by Bombrun *et al.* to model the polarimetric vector data[12]. We use its multilook extension, named the multivariate $\mathcal{U}_d$-distribution, for multilook covariance matrix data. The flexibility of this model with respect to $\mathcal{K}_d$ and $\mathcal{G}_d^0$ with an extra texture parameter encourages the authors to use this model for multitemporal multipolarization SAR data. It is expected to yield improved results because of its flexibility to model more varied textures. Using the matrix log-cumulant diagram [13], we demonstrate the capability of the multivariate $\mathcal{U}_d$-distribution to model multipolarization SAR data.

In this study, we use an unsupervised contextual non-Gaussian clustering algorithm, named $\mathcal{U}$-MRF in [14], to segment each terrain corrected SAR scene. This contextual non-Gaussian clustering algorithm uses a Markov random field (MRF) model that integrates the $\mathcal{U}_d$-distribution for the multipolarization SAR data statistics conditioned to each image cluster, and a Potts model for the spatial context. The parameters of the $\mathcal{U}$-MRF model are estimated by the iterative expectation-maximization (EM) algorithm [15] and Besag's algorithm [16] in the segmentation process. Contextual information can improve the accuracy and robustness of the image segmentation and hence leads to improved change detection results. The theoretical approach proposed in this paper is general for multipolarization SAR data and applicable to dual polarization and single polarization SAR data, although with some restrictions.

The analysis utilizes several ENVISAT ASAR, dual polarization scenes over Kongsvegen glacier, Svalbard from spring 2004, 2005 and 2006, together with some ground based field observations. Ground truth data are used to label segmented images and to investigate the accuracy of classifications. We demonstrate consistency by comparing classified scenes taken on the same day and from different acquisition parameters (e.g., look angle). The surface of a glacier can be roughly divided into accumulation and ablation areas, separated by the equilibrium line (the dividing line between the accumulation and ablation areas) [17]. Monitoring the firn line position over time is of interest, because there are indications that this line is correlated with the equilibrium line. Hence, we demonstrate the consistency of the classification results as firn area total variation between chosen no change pairs to obtain the expected variation of firn area boundary with superimposed ice (SI) zone. Subsequent yearly classifications are discussed in terms of post-classification change detection and changes are identified as the detected difference in the locations of boundaries between glacier facies.

This paper is organized as follows: In Section II, we define the backscatter quantities measured by a PolSAR, namely the scattering matrix, radar backscatter, and the area normalized scattering vector. Section III describes the processing chain of time series analysis including multilook processing, terrain correction, PDF selection, unsupervised segmentation and post-classification change detection. Section IV introduces the study area and describes the example data. Section V demonstrates the results. Finally, conclusions from the presented research are given in Section VI.

II. Measurements from SAR Sensors

A full-polarimetric imaging radar measures the amplitude and phase of backscattered signals in the four combinations of the linear receive and transmit polarizations: HH, HV, VH, and VV. These signals are used to form a complex scattering matrix, denoted $\mathbf{S} = [S_{rt}] \in \mathbb{C}^{2\times 2}$, associated with each resolution cell in the image, which relates the incident and the scattered electromagnetic fields as follows [18]

$$\begin{bmatrix} E_h^s \\ E_v^s \end{bmatrix} = \frac{e^{-jkR}}{R} \begin{bmatrix} S_{hh} & S_{hv} \\ S_{vh} & S_{vv} \end{bmatrix} \begin{bmatrix} E_h^i \\ E_v^i \end{bmatrix}. \quad (1)$$

Here k denotes the wavenumber, R is the (radial) distance between the radar antenna and target, and $j = \sqrt{-1}$ is the imaginary unit. The superscript of the electromagnetic field components indicates incident (i) or scattered (s) wave. The term $\frac{e^{-jkR}}{R}$ takes into account the propagation effects both in amplitude and phase. The scattering matrix $\mathbf{S}$, which holds the scattering coefficients in (1), can be vectorized and represented as the scattering vector $\underline{\mathbf{S}}$

$$\underline{\mathbf{S}} = [S_{hh}, S_{hv}, S_{vh}, S_{vv}]^T \in \mathbb{C}^4, \quad (2)$$

where the superscript T denotes the transpose of a vector or a matrix. Assuming that the target reciprocity condition is satisfied (i.e., $S_{hv} = S_{vh}$), the lexicographic scattering vector, $\underline{\mathbf{\Omega}}$, with dimension $d = 3$ can be extracted from the scattering matrix as

$$\underline{\mathbf{\Omega}} = [S_{hh}, \sqrt{2}S_{hv}, S_{vv}]^T \in \mathbb{C}^3, \quad (3)$$

where the elements represent the complex backscattering coefficients in the three polarimetric channels, and $\sqrt{2}$ arises from the requirement to conserve the total scattered power. The vectors $\underline{\mathbf{S}}$ and $\underline{\mathbf{\Omega}}$ are single-look complex (SLC) format representations of polarimetric SAR data. Single and dual-channel polarimetric data can be treated in a similar way as subsets of lesser dimension, and, most likely, proportionally less information.

The radar backscatter (β) of a given target measured in the range-azimuth coordinates for linear polarizations $r, t \in \{H, V\}$ can be obtained from the elements of scattering matrix in (1) as follows [19]:

$$\beta_{rt} = 4\pi |S_{rt}|^2. \quad (4)$$

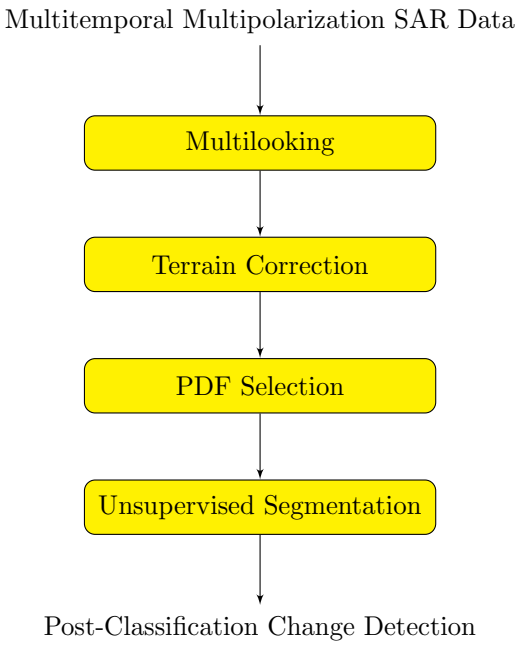

Fig. 1. Processing chain of time series analysis for post-classification change detection.

Both S_{rt} and β_{rt} are functions of spatial position, wave frequency, viewing geometry, wave polarization, geometrical structure and dielectric properties of the object [18]. Expressions (1)–(4) above represent the quantities which are directly measurable by a SAR sensor. The area normalized scattering vector in the slant range plane (subscript β) is defined as:

$$\underline{\mathbf{\Omega}}_{\beta^0} = \frac{\underline{\mathbf{\Omega}}_{\beta}}{\sqrt{A_\beta}}, \tag{5}$$

where A_β represents the reference area of the β^0 backscatter coefficient that contributes to the recorded signal.

Fully-polarimetric data is not always available because the wider coverage of dual polarization or single polarization modes are often preferred for monitoring purposes such as change detection. The different possible configurations of the dual polarization mode systems are: HH/HV, VV/VH, or HH/VV. Therefore, only a reduced version of $\underline{\mathbf{\Omega}}$ is available. Single channels are also possible, generally in HH or VV.

III. Processing Chain for Post-Classification Change Detection

The time series analysis of multitemporal multipolarization SAR data for post-classification change detection in this study consists of a processing chain with five stages, as depicted in Fig. 1, which can be used for both single- and multi-channe SAR data. These stages are explained in detail bellow. The inputs are multitemporal multipolarization SAR images with different configurations.

A. Stage 1: Multilooking

To utilize the multitemporal polarimetric acquisitions, the scattering vectors for all acquisitions have to be co-registered. These scattering vectors are transformed into the form of multilooked sample covariance matrices in order to reduce speckle noise at the expense of spatial resolution, i.e., [18]

$$\mathbf{C} = \frac{1}{L}\sum_{\ell=1}^{L} \underline{\mathbf{\Omega}}_\ell \underline{\mathbf{\Omega}}_\ell^H, \tag{6}$$

where L is the nominal number of looks used for averaging, $(\cdot)^H$ means the Hermitian transposition operator. Hence, after multilooking, each pixel in the image is a realization of the $d \times d$ stochastic matrix variable denoted $\mathbf{C}$, and the image is referred to as the multilook complex (MLC) covariance image. Note that the multilooking is performed as a type of speckle filtering, a simple boxcar filter. Some of the more advanced speckle filters cannot be applied because they invalidate the statistical modelling that is performed in the next stages.

B. Stage 2: Terrain Correction

Terrain topography influences both the placement of each observed point on the Earth's surface and the brightness of the radar return in radar geometry [20], [21]. In this stage, we implement a three-step method to generate terrain corrected polarimetric SAR images for time series analysis. The procedure consists of the following steps:

- Geometric terrain correction (GTC)
- Radiometric terrain correction (RTC)
- Orientation angle Compensation (OAC)

B.1 Geometric Terrain Correction (GTC)

The objective of SAR geocoding is to find the corresponding position on the Earth for each image pixel, thereby transforming from the SAR coordinate image into an Earth-based coordinate image. Since the satellite state vector is known from the orbit information, the position of each SAR pixel is estimated for a given earth model by solving the so-called *range-Doppler* equations [22]. Due to geometrical distortions caused by the side-looking geometry and rugged terrain, a one-to-one relation does not always exist between the radar and the geographic map coordinates [3]. Those pixels that are located in layover and radar shadow regions have to be masked out in this step. The importance of accurate geocoding of multitemporal imagery is obvious because largely spurious results of change detection will be produced if there is misregistration. In cases of misregistration, a number of false alarms, especially in the region of rapid intensity change such as edges, occur. This necessitates the use of precise terrain geocoding of SAR data that not only registers the images to a standard map projection by using a high resolution DEM and precise orbital information, but also performs the GTC.

B.2 Radiometric Terrain Correction (RTC)

The normalization of SAR imagery for systematic terrain variations is required for meaningful single sensor multi-track intercomparisions and post-classification change detection. Although the position of the backscatter

estimate has been corrected by the GTC, the radiometry of the goecoded image remains in the slant range plane. Therefore, RTC is applied to correct distortions due to the side-looking geometry of SAR systems and hill-slope modulations. In this study, we first normalize the scattering coefficients with respect to the β_0 reference area (A_β) according to (5), and then apply the radiometric slope correction factor, $\cos(\Psi)$, proposed in [2], on the covariance matrices. Provided that the data are already calibrated with respect to the elevation antenna pattern, range spreading loss, and channel to channel calibration, all elements of covariance matrix in (6) can be simultaneously radiometrically corrected to the ground range area by

$$\mathbf{C}_{\mathrm{RTC}} = \frac{\cos(\Psi)}{L}\sum_{\ell=1}^{L}(\underline{\mathbf{\Omega}}_{\beta^0})_\ell(\underline{\mathbf{\Omega}}_{\beta^0})_\ell^H = \cos(\Psi)\cdot\mathbf{C}_{\beta^0}, \quad (7)$$

where the Ψ is the projection angle between the surface normal and the image plane normal, which is assumed to vary between 0° and 90° and exclude layover areas [2].

All covariance matrix values now correspond to the σ^0 backscatter coefficient, which is equivalent to $\sigma^0 = \beta^0 \cdot \cos(\Psi)$. The conventional radiometric normalization method, which relies on the local incidence angle only, is adequate for flatlands or for pixels with zero slope. The expected results are radiometrically "flattened" SAR images. The required parameters for performing the RTC are estimated in the geocoding step using an available DEM and satellite state vector. In cases of unavailable DEM, ellipsoidal-based radiometric correction is achieved over an earth model such as WGS-84.

B.3 Orientation Angle Compensation (OAC)

Since different scattering mechanisms (double bounce, surface scattering, and volume scattering) have different sensitivity to terrain topography, RTC is not sufficient for polarimetric applications to produce reliable results for scattering characteristics [6]. The last step of terrain correction is to compensate the polarization signature which is due to topography effects, specifically azimuth slope variations. Polarization orientation angle (POA) shifts are introduced by terrain topography slopes in the azimuth direction. These shifts make the covariance matrix *reflection asymmetric* and can be compensated based on the derived POA by DEM in [5]. When a DEM is not available, target decomposition-based methods are an alternative to estimate the azimuth slope induced POAs directly from polarimetric SAR data [23]. After deriving the POA, the compensation can be done on all elements of the covariance matrices by

$$\mathbf{C}_{\mathrm{OAC}} = R(\vartheta)\mathbf{C}_{\mathrm{RTC}}R^T(\vartheta) \quad (8)$$

where ϑ is the shift in the POA required to achieve the maximum co-polarization response, $R(\vartheta)$ denotes the rotation matrix [7], and $\mathbf{C}_{\mathrm{RTC}}$ and $\mathbf{C}_{\mathrm{OAC}}$ are the covariance matrix before (after the RTC) and after rotation, respectively.

For most natural backscatter media reflection symmetry holds, meaning that the co- and cross-polarized channels are uncorrelated. However, azimuth slope variations may induce correlation between these channels. Subsequently, the OAC over images leads to reflection symmetric covariance matrix data. The data are now ready for quantitative image analysis, such as surface cover change detection.

C. Stage 3: PDF Selection

C.1 The Multilook Product Model

The multilook polarimetric product model describes the terrain corrected covariance matrix $\mathbf{C}$ as the product of two independent stochastic variables [8], [11] as

$$\mathbf{C} = Z\mathbf{W}, \quad (9)$$

where the strictly positive, unit mean scalar random variable Z models texture, and represents the backscatter variability due to heterogeneity of the radar cross section. The texture term is scalar because of the assumption of equal textural variations for all polarimetric channels. The second contribution, the speckle term $\mathbf{W}$, follows a scaled complex Wishart distribution [13], denoted $s\mathcal{W}_d^{\mathbb{C}}(L,\mathbf{\Sigma})$, with parameters L, the number of looks, and the scale matrix with $\mathbf{\Sigma} = E\{\mathbf{W}\}$. The marginal distribution for $\mathbf{C}$ may be derived by integrating the conditional PDF over the prior distribution of Z, that is

$$p_C(\mathbf{C}) = \int_0^\infty p_{C|Z}(\mathbf{C}|z)p_Z(z)dz, \qquad \mathbf{C}|z \sim s\mathcal{W}_{\mathbb{C}}^d(L, z\mathbf{\Sigma}). \quad (10)$$

The PDF of $\mathbf{C}$ depends on the specific model for the scalar texture variable Z [8], [9]. The simplest multilooked PolSAR model for the PDF of $\mathbf{C}$ is achieved with a constant texture parameter (i.e., PDF of Z is Dirac delta function, $\delta(z-1)$) which is justified only for homogeneous regions of the image, and leads to the scaled complex Wishart distribution [13]. For areas with pronounced texture, non-Gaussian probability distributions provide better representation of the data. If the texture random variable is gamma distributed, the covariance matrix $\mathbf{C}$ follows the well-known $\mathcal{K}_d$-distribution [24], [8]. The $\mathcal{G}_d^0$-distribution is another multivariate distribution [11], [25], which implies an inverse gamma distributed texture. The two parameter multivariate Kummer-U distribution has been introduced in [12] to generalize the above mentioned PDFs to model PolSAR vector data which implies a unit mean Fisher-Snedecor (FS) distributed texture with PDF given by [26]

$$p_Z(z;\xi,\zeta) = \frac{\Gamma(\xi+\zeta)}{\Gamma(\xi)\Gamma(\zeta)}\frac{\xi}{\zeta-1}\frac{\left(\frac{\xi}{\zeta-1}z\right)^{\xi-1}}{\left(\frac{\xi}{\zeta-1}z+1\right)^{\xi+\zeta}}. \quad (11)$$

$\xi > 0$ and $\zeta > 0$ are called the shape parameters. The flexibility of the FS distribution is controlled with these shape parameters to steer between the heavy head and heavy tail distributions. Lower values of ξ and ζ represent significant texture and higher values represent low texture.

Where the resulting $\mathcal{U}_d$-distribution for $\mathbf{C}$ is parameterized $\mathcal{U}_d(L,\mathbf{\Sigma},\xi,\zeta)$ and is given in closed form as [27]

$$p_{\mathbf{C}}(\mathbf{C}) = \frac{L^{Ld}}{\Gamma_d(L)}\frac{|\mathbf{C}|^{L-d}}{\mathbf{\Sigma}^L}\frac{\Gamma(\xi+\zeta)\Gamma(Ld+\zeta)}{\Gamma(\xi)\Gamma(\zeta)}\left(\frac{\xi}{\zeta-1}\right)^{Ld} \times U\left(Ld+\zeta, Ld-\xi+1, L\mathrm{tr}(\mathbf{\Sigma}^{-1}\mathbf{C})\frac{\xi}{(\zeta-1)}\right), \tag{12}$$

where $\mathrm{tr}(\cdot)$ and $|\cdot|$ denote the trace and determinant operators, respectively, d is the number of polarimetric channels, and $\Gamma_d(L)$ is a normalization constant

$$\Gamma_d(L) = \pi^{\frac{d(d-1)}{2}}\prod_{i=1}^{d}\Gamma(L-i+1). \tag{13}$$

$\Gamma_d(\cdot)$ is named the multivariate gamma function of the complex kind in [13], while $\Gamma(\cdot)$ is the standard Euler gamma fuction. $U(\cdot,\cdot,\cdot)$ denotes the confluent hypergeometric function of the second kind (KummerU). $L \geq d$ ensures that $\mathbf{C}$ is nonsingular.

C.2 Parameter Estimation of the $\mathcal{U}_d$-Distribution

Based upon Mellin transform theory, in [13] the method of matrix log-cumulants (MoMLC) has been proposed to estimate the shape parameters of the Fisher PDF. It has proved to be an effective estimation approach associated with the multilook product model. More details on the MoMLC for parameter estimation of the $\mathcal{U}_d$ model can be found in [13]. It is essentially a minimum distance search in the log-cumulant domain.

C.3 Evidence for $\mathcal{U}_d$-Distribution

The matrix log-cumulant diagram, which was proposed by Anfinsen and Eltoft in [13] as a visualization tool for textured multilook multipolarization SAR data, is used to compare data with the potential distribution models. It is expected that $\mathcal{U}_d$ can be a suitable PDF for polarimetric SAR scenes because of its flexibility to capture highly varied textures and to model both heterogeneous and homogeneous clutter. In addition, it includes the s$\mathcal{W}_d$, $\mathcal{K}_d$, $\mathcal{G}_d^0$ as asymptotic cases as follows:

$$\begin{aligned}
&\lim_{\zeta\to\infty}\mathcal{U}_d(L,\mathbf{\Sigma},\xi,\zeta) = \mathcal{K}_d(L,\mathbf{\Sigma},\alpha),\\
&\lim_{\xi\to\infty}\mathcal{U}_d(L,\mathbf{\Sigma},\xi,\zeta) = \mathcal{G}_d^0(L,\mathbf{\Sigma},\eta),\\
&\lim_{\xi\to\infty,\zeta\to\infty}\mathcal{U}_d(L,\mathbf{\Sigma},\xi,\zeta) = s\mathcal{W}_d^{\mathbb{C}}(L,\mathbf{\Sigma}),
\end{aligned} \tag{14}$$

where α and η denote the texture parameters of the $\mathcal{K}_d$ and $\mathcal{G}_d^0$ distributions, respectively.

D. Stage 4: Unsupervised Segmentation

An unsupervised, non-Gaussian, contextual segmentation method is used that combines an advanced statistical distribution with spatial contextual information for MLC data. It is based on a Markov random field (MRF) model that integrates a $\mathcal{U}_d$-distribution for the polarimetric SAR data statistics conditioned to each image cluster and a Potts model for the spatial context [14], [28]. Specifically, the proposed algorithm is constructed based upon the expectation maximization (EM) and Besag's algorithms. The resulting algorithm works in an iterative manner to jointly address parameter estimation of the $\mathcal{U}_d$-distribution and the spatial context model, and also minimization of the energy function [29]. Specifically, this method incorporates the information about spatial context for the purpose of reducing the effect of speckle noise. More details about the clustering algorithm can be found in [14]. We obtain unlabeled segmentation results which then need additional knowledge to align classes for comparison. Therefore, ground truth data are used to label segmented images and also to obtain overall classification accuracies.

E. Stage 5: Post-Classification Change Detection

Post-classification change detection can be viewed as a particular case of the multitemporal image classification problem. This approach for change detection requires very high accuracy of the classification results from the previous stage. We believe that by using the unsupervised contextual non-Gaussian segmentation method on terrain corrected SAR scenes results in a robust segmentation which improves also the reliability of change detection. Since the class labels match on all images, we investigate changes for consistency and post-classification comparison change detection. The consistency of the segmentation method is characterized by comparing segmentation results of scenes taken on the same day (assumed 'no change') with different acquisition parameters. This allows us to determine whether an observed variation is statistically significant and therefore can be used for post-classification change detection of Arctic glaciers. Subsequently, the classified images of succeeding years are compared, and changes are identified as the detected differences in the location of boundaries between glacier facies. The differences between classified pairs can only be considered significant change when compared to that of the classification total variation.

IV. Study Area and Data set Description

The glacier Kongsvegen situated at approximately 78° 50′ N and 13° E in the northwest of Spitsbergen, Svalbard, close to the meteorological station Ny-Ålesund is selected for the workflow presented in Section III. Kongsvegen is a surge-type glacier about 25 km long, covers an area of approximately 100 km^2, and is oriented in a northwest–southeast direction extending from an elevation of 800 m a.s.l to sea level. The glacier has a flow velocity of < 4 m a^{-1} and is thus a very slow moving glacier.

The satellite data set consists of a time series of correctly calibrated acquired SAR images for the period 2004-2006 over glacier. The images are generally collected under different acquisition configurations. The series consists of dual polarization C-band ENVISAT-advanced-synthetic-

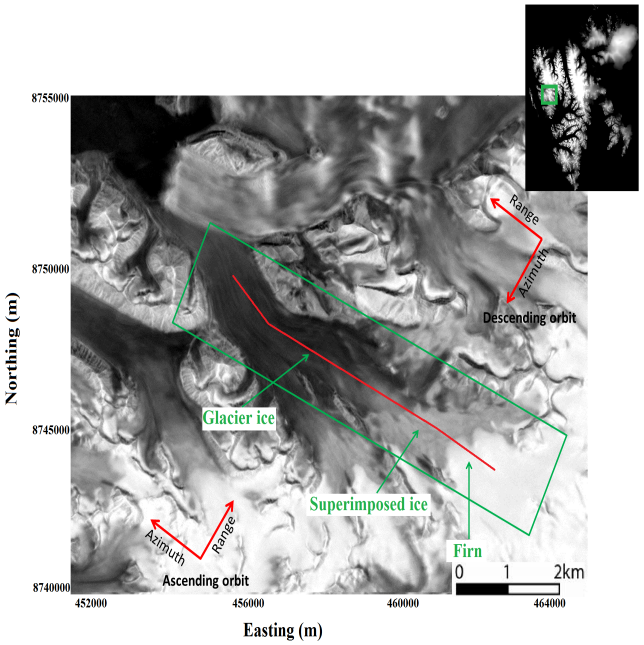

Fig. 2. SAR intensity image of field site Kongsvegen (shown on a UTM grid projection) located on the northwest of Svalbard (inset). The three zones of interest, glacier ice, superimposed ice, and firn, can be visibly identified by their dark, medium, and bright intensities, respectively. The green frame shows the area of interest to be analyzed further. The glacier center line extends from the firn area (lower right) into the glacier ice zone (upper left).

aperture-radar (ASAR) images in alternating polarization (AP) mode from both ascending and descending orbits and in both HH/HV and VV/VH polarizations, over a large range of look angles from 14 to 43 degrees (swath angles IS1 to IS7). As seen in Fig. 2, the satellite flight path is across glacier with the SAR looking down glacier for a descending orbit. In ascending orbits, the satellite track is approximately parallel to glacier center line; thus, the SAR look direction is across glacier. The initial resolution of the raw SAR SLC images is 7.8 m in the slant range and 3.2 m in the azimuth direction. The SAR intensity image in Fig. 2 shows the spatial variability of the three different distinct zones across the glacier. Each zone has specific backscatter characteristics. In the upper parts of the glacier where firn accumulation occurs, layers dominated by large firn grains and ice layers cause considerable volume scattering on the ENVISAT SAR wavelength leading to high backscatter [30]. The SAR signature in the ablation area is dominated by backscatter from the previous summer surface. In the SI area, varying fractional volumes of bubbles cause coherent and incoherent scattering likely causing of medium backscatter values. Although the previous summer surface still contributes, the increase in total backscatter, which determines glacier ice (GI) from SI, is caused by the air bubbles [17]. The GI does not reflect much of the incoming SAR signal back to the sensor, resulting in low backscatter values.

A DEM of 20 m pixel resolution covering all of Svalbard was also available, which was produced by the Mapping Section of the Norwegian Polar Institute (NPI). Ground truth data are derived from a network of C-band ground penetrating radar (GPR) profiles oriented parallel to the glacier center line collected by the NPI in 2005 under the same spring conditions as the ASAR images. GPR is commonly used in glaciology for mapping layers within the glacier such as internal accumulation layers and the previous summer surface, as well as bedrock topography [31]. The differential GPS (DGPS) was used to determine the position of the GPR profiles with a horizontal accuracy within 10 cm. The C-band GPR is a step-frequency continuous-wave (SFCW) radar operating at 4.8-5.8 GHz. The center frequency of 5.3 GHz is the same as the ASAR instrument onboard ENVISAT [32]. Details of the GPR data are given in [32], [33]. The along glacier profiles have been manually classified into three zones of interest, i.e., GI, SI, and firn.

TABLE I
SUITABLE ENVISAT C-BAND SAR SCENES WITH DIFFERENT ACQUISITION CONFIGURATIONS FOR TIME SERIES ANALYSIS.

Image no	Date	Look angle	Path	Polarizarion
I_1	04 May 2004	IS3	des	VV/VH
I_2	05 May 2004	IS5	des	HH/HV
I_3	05 May 2004	IS7	asc	VV/VH
I_4	09 May 2004	IS5	asc	VV/VH
I_5	10 May 2004	IS3	asc	VV/VH
I_6	28 Dec 2004	IS2	des	VV/VH
I_7	02 Feb 2005	IS2	asc	VV/VH
I_8	09 Mar 2005	IS2	asc	VV/VH
I_9	11 Apr 2005	IS7	des	VV/VH
I_{10}	13 Apr 2005	IS2	asc	VV/VH
I_{11}	14 Apr 2005	IS6	asc	VV/VH
I_{12}	15 Apr 2005	IS4	asc	VV/VH
I_{13}	17 Apr 2005	IS6	des	VV/VH
I_{14}	17 Apr 2005	IS7	asc	VV/VH
I_{15}	18 Apr 2005	IS4	asc	HH/HV
I_{16}	19 Apr 2005	IS3	des	HH/HV
I_{17}	21 Apr 2005	IS1	des	HH/HV
I_{18}	27 Apr 2005	IS7	des	VV/VH
I_{19}	28 Apr 2005	IS2	des	VV/VH
I_{20}	28 Apr 2005	IS3	asc	VV/VH
I_{21}	29 Apr 2005	IS1	asc	VV/VH
I_{22}	29 Apr 2005	IS4	des	VV/VH
I_{23}	30 Apr 2005	IS6	asc	HH/HV
I_{24}	01 May 2005	IS2	des	VV/VH
I_{25}	01 May 2005	IS4	asc	VV/VH
I_{26}	02 May 2005	IS2	asc	VV/VH
I_{27}	03 May 2005	IS6	des	HH/HV
I_{28}	05 May 2005	IS3	des	VV/VH
I_{29}	17 May 2005	IS2	des	VV/VH
I_{30}	21 Feb 2006	IS2	des	VV/VH
I_{31}	15 Apr 2006	IS6	asc	HH/HV
I_{32}	16 Apr 2006	IS2	des	VV/VH
I_{33}	17 Apr 2006	IS2	asc	VV/VH
I_{34}	19 Apr 2006	IS4	asc	VV/VH
I_{35}	20 Apr 2006	IS2	asc	VV/VH
I_{36}	20 Apr 2006	IS3	des	VV/VH

Meteorological conditions also affect the backscatter in addition to the SAR imaging geometry and surface topography effects as discussed in Section III-B. Therefore, from temperature and precipitation observations of Ny-Ålesund station, located at sea level about 15 km west of the terminus of Kongsvegen, we select only SAR images collected in

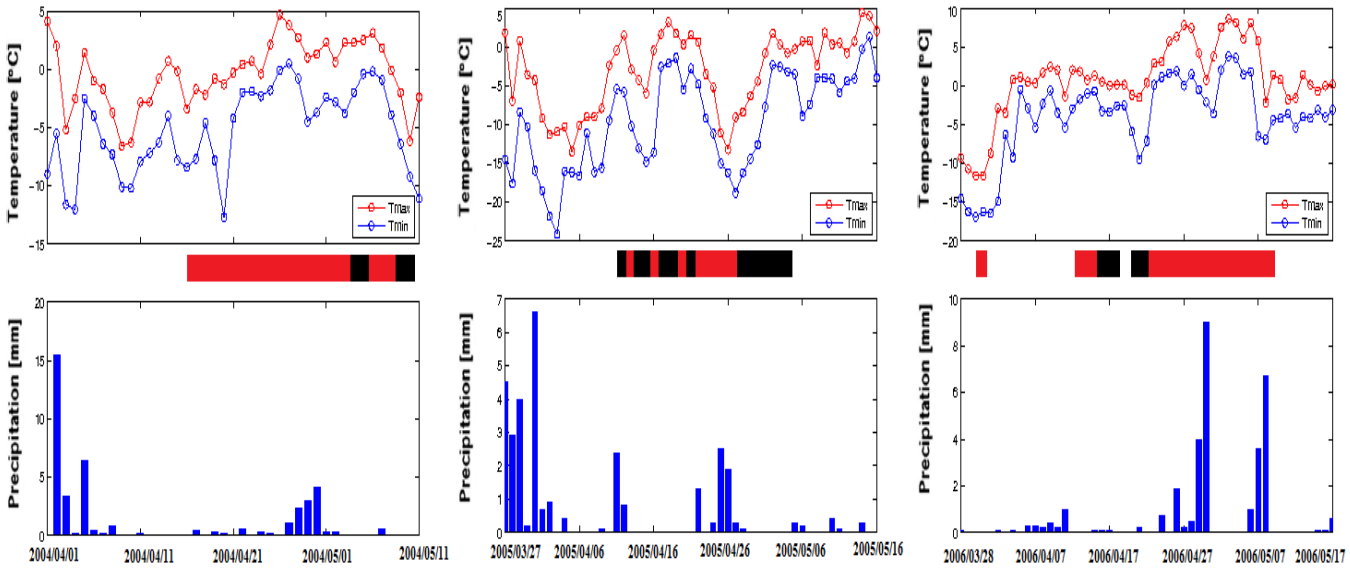

Fig. 3. Daily air temperature and precipitation observed in Ny-Ålesund between 2004-2006. Data are from the Norwegian Meteorological Institute. The black/red bars between the temperature and precipitation represents times of SAR acquisition. The black bars indicate the chosen SAR images based on the temperature and precipitation constraints, listed in Table I, for time series analysis.

spring under cold and dry conditions on the glacier surface, see Fig 3. In cases of wet conditions, scattering occurs only at the wet-snow surface and the underlying GI has no of influence on the measurements. When just a small amount of liquid water is present in the upper layer of snow and firn, the radar backscatter properties change significantly [30]. However, in early spring the snow pack on the glacier surface is mostly dry and the previous summer surface at the base of the winter snow pack gives the strongest return. Thus this is the time of the year that the SAR signal incorporates the longer time scale signal is recommended to collect the SAR data for monitoring temporal changes of the glacier [33]. We refer readers to [34] to show the influence of wet conditions on radar response. The authors demonstrated a good example image coinciding with the onset of rain in the meteorological records and an image taken after the onset of rain clearly showed significant change compared to the day before. The suitable SAR images are chosen based on the temperature and precipitation constrains. The remaining images for the time series analysis are listed in Table I.

V. Experimental Results

We now use the proposed workflow in Section III to analyze multitemporal dual polarization SAR data for glacier change detection.

The raw SLC data are geocoded and multilooked simultaneously to a final geocoded resolution of approximately 30 x 30 m. The SLC image pixels were multilook averaged with 2 looks in the range direction and 12 looks in the azimuth, 24-looks in total. We have chosen 24-looks for the multilooking because it is a moderately large degree of multilooking and would achieve a high degree of speckle reduction. The 30 m ground resolution is good enough for the monitoring purpose in glacier areas.

The reconstruction of radar geometry with the help of DEM, the known orbit data vector, and image-line timing is done for each ASAR image. This stage not only derives the geocoding look-up tables, but also derives various geometrical parameters for each ground point that are required for terrain corrections, such as local incidence angle, and also generates the layover-shadows mask. The pixels affected by the geometrical distortions are mainly located at slopes larger than 40 degrees. Kongsvegen glacier has a gentle surface slope of 0.5-5 degrees and, therefore, such geometric corrections will be minimal over the glacier region.

The radiometric normalization of the covariance matrix data was then applied for each scene. Although the glacier slopes are generally small, if left uncorrected they may manifest as misclassification of the glacier class boundaries. The projection factor is shown in Fig. 4(c) as an example. The backscatter coefficient is reduced when using the projection factor to radiometrically correct the covariance matrix data. The negative projection factors (the projection angles larger than 90 degree), correspond to the dark blue areas in Fig. 4(c) and red areas in the slope map. These areas are mostly affected by layover and in the geocoding step have to be masked out, as seen in Fig. 4(b). The DEM-derived POAs are used to correct for the azimuth slope effect on the polarization signature. By estimating the POA for the data, see Fig. 4(d), we observe that for the rugged-terrain areas surrounding the glacier, the polarization shifts are more significant. Subsequently, the OAC over images leads to reflection symmetric covariance matrix data sets.

To demonstrate the effect of both RTC and OAC on the covariance matrix data, the profile along the glacier center line was plotted for the four images with different geometries. It should be mentioned that the middle of the

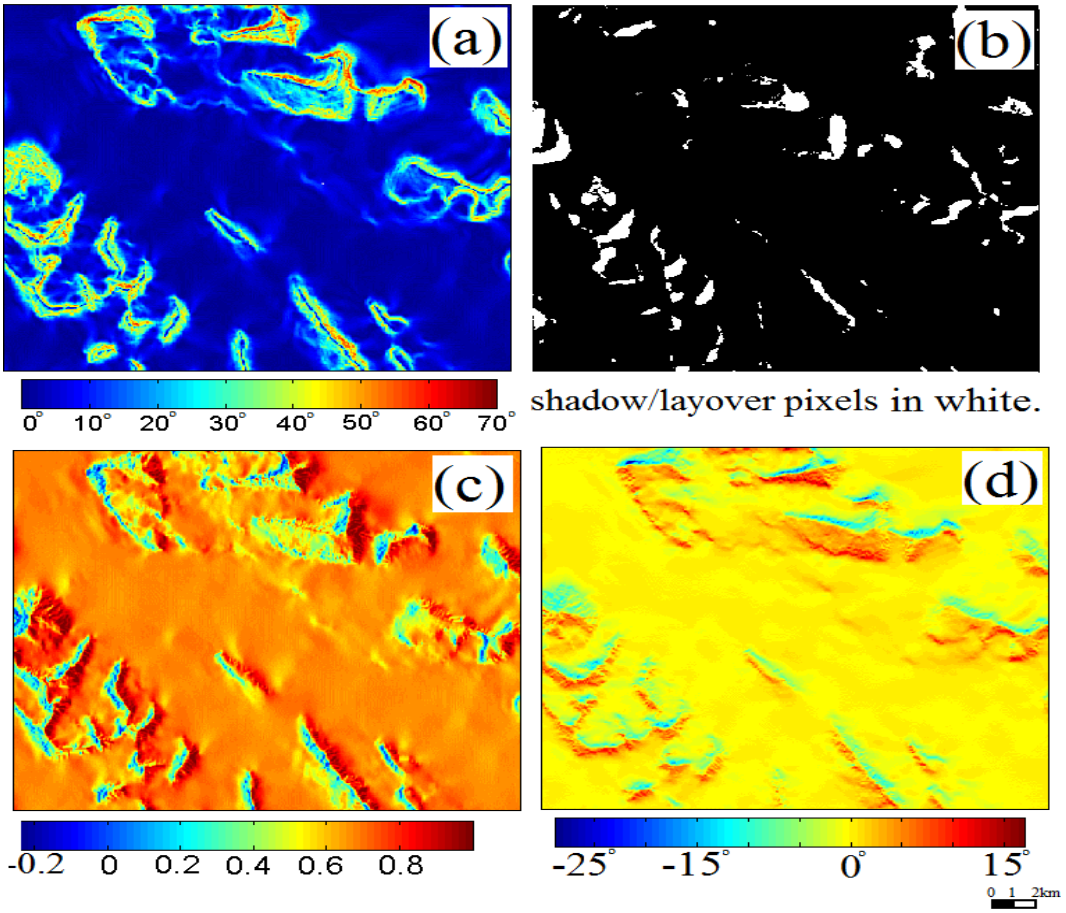

Fig. 4. Terrain correction parameters of the covered area in the map geometry. (a) slope angle map in degrees (b) shadow/layover mask produced from the geocoding step (c) projection factor (d) the DEM-derived POA in degrees.

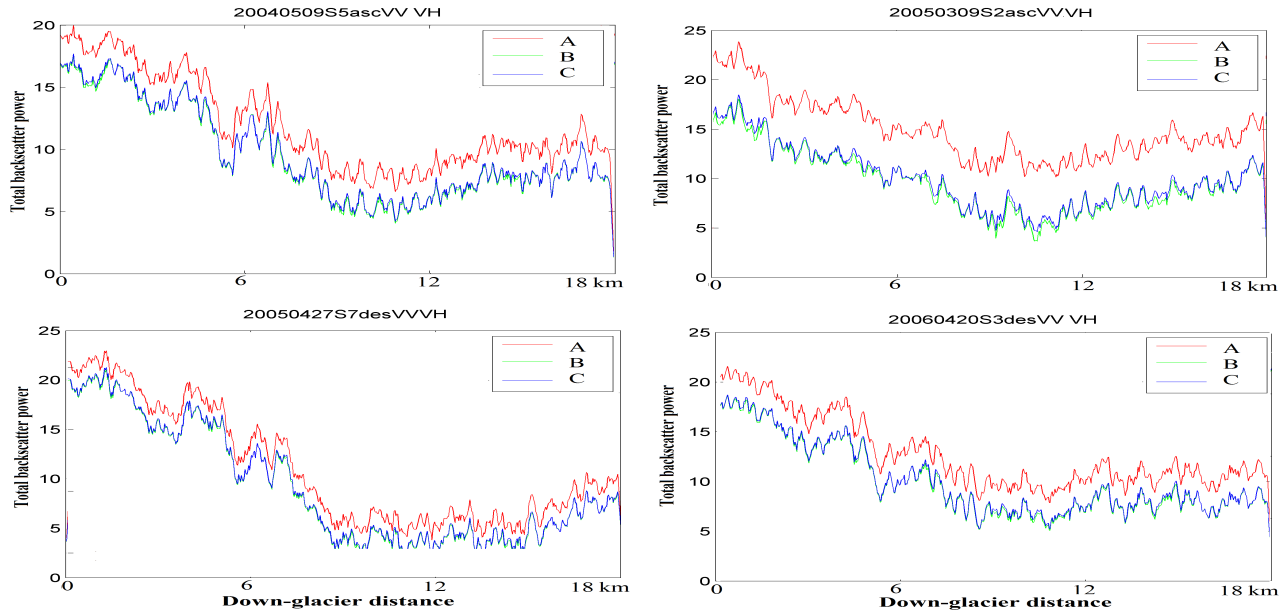

Fig. 5. The effect of terrain correction on dual polarization ASAR data for the four candidate images with different geometries: before radiometric normalization (A); after radiometric normalization (B); and after the OAC with DEM (C) along the glacier center line extending from the the firn area into GI zone.

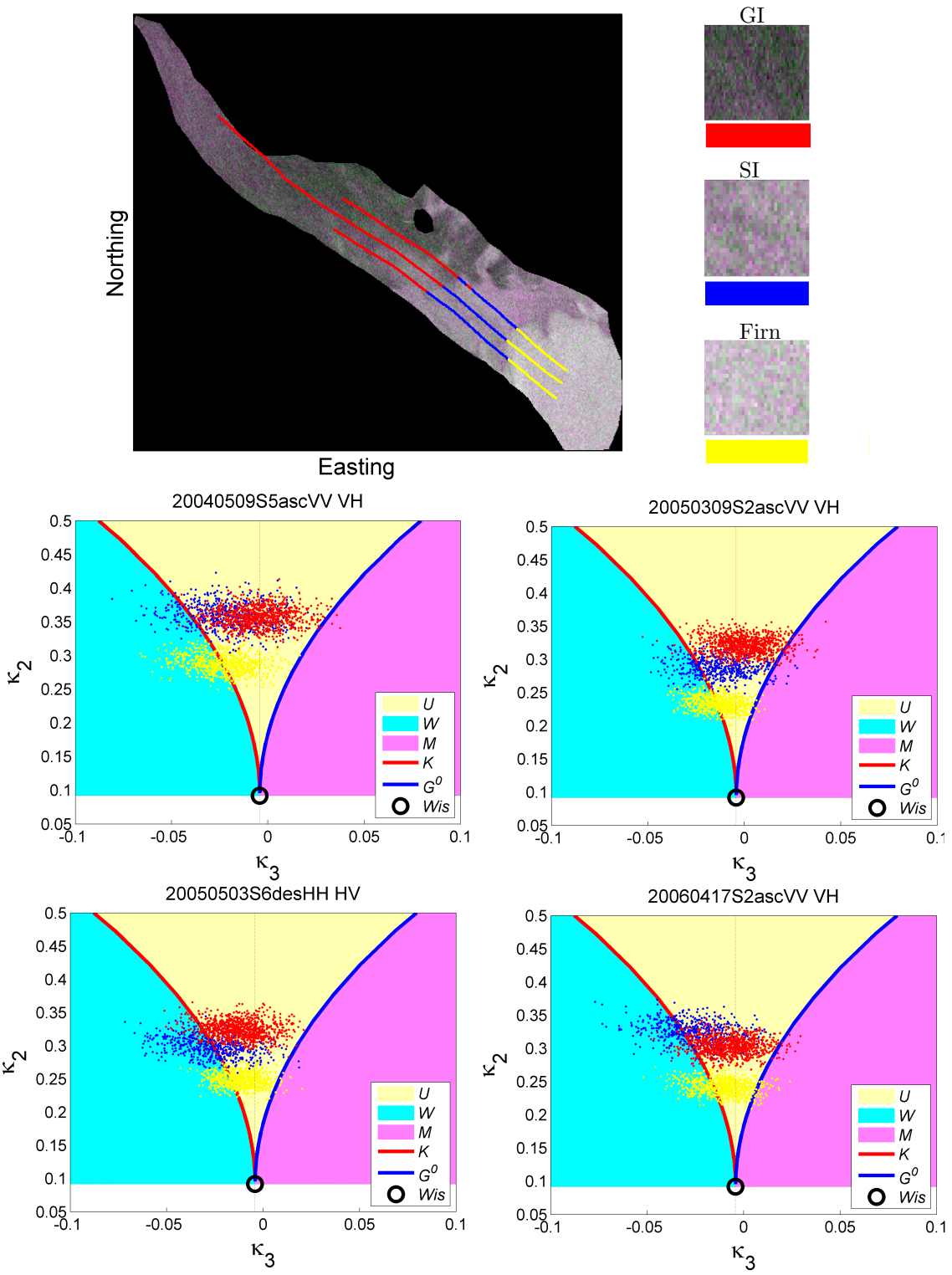

Fig. 6. (Top) An example of Quasi-Pauli RGB images of Kongsvegen glacier from 2005 with GPR derived ground truth overlaid. Legend on the right shows homogeneous samples of different glacier zones along with class label colors: red =GI, blue = SI, and yellow = firn. (Bottom) matrix log-cumulant diagrams: κ_3/κ_2 estimation for the candidate terrain corrected images are estimated from the image samples. The cluster centers seem to fall within the $\mathcal{U}_d$-distribution region in the diagrams. The variables of the diagrams are defined in the text. The elliptical scatter clouds indicates the natural variation in the measure due to finite sample size estimation.

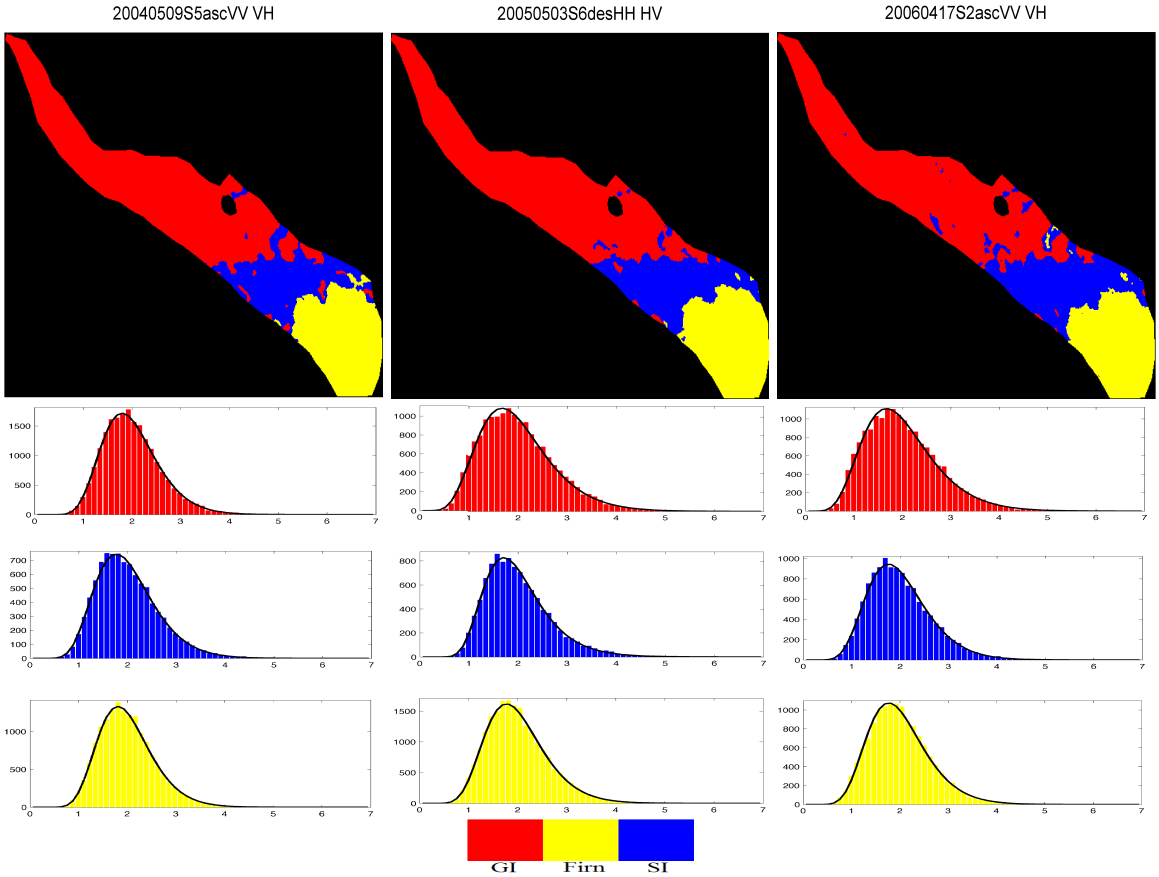

Fig. 7. (Top) unsupervised segmentation of the candidate images for each year (2004, 2005, and 2006), (bottom) comparison between fitted models and class histograms of trace($\mathbf{\Sigma}^{-1}\mathbf{C}$) for all classes, the figures show the good visual fit of the $\mathcal{U}$-MRF model to all class histograms.

three GPR ground truth lines in Fig. 6 follows the glacier center line extending from the firn area into the GI zone. The original backscatter coefficient, RTC and OAC values are shown with red, green and blue lines respectively. The reduction of backscatter coefficient is geometry-dependent which shows the suppression of the SAR geometry effects on the data such that the images are comparable for the monitoring purpose. For example, the offset between original backscatter and RTC backscatter for the look angle IS1 is larger than look angle IS7, see Fig. 5. The total backscatter power (Span=$C_{11} + C_{22}$) in Fig. 5 does not change significantly after OAC except some small changes for the pixels located at the higher azimuth slopes. For those pixels, the total power increased after the OAC.

To evaluate the capability of the $\mathcal{U}_d$ PDF to model the variable texture of the polarimetric SAR data set, the second and third sample log-cumulants (κ_3, κ_2) are computed on a sliding window of size 5×5 [26]. Matrix log-cumulant diagrams are plotted for each scene of the multitemporal data, see Fig. 6. In the diagrams, the $\mathcal{K}_d$ and $\mathcal{G}_d^0$ are represented by the red and blue curves, respectively. The junction of two curves is the point which represents the non-textured s$\mathcal{W}_d$ PDF. The $\mathcal{U}_d$-distribution covers the light yellow space between the red and blue curves. The Whittaker $\mathcal{W}$ and $\mathcal{M}$ PDFs are not considered in this study. The clusters of sample matrix log-cumulants plotted in Fig. 6 represent targets that have been selected from four example scenes with different configurations. In the diagrams, the collection of sample matrix log-cumulants for the firn, SI, and GI samples are shown as yellow, blue, and red dots, respectively. The variation in the clusters for each zone in the different scenes reveals that the statistical texture properties are dependent on external factors like the acquisition geometry. The cluster centers, and hence the data model, seem to fall within the $\mathcal{U}_d$-distribution region, even though some of the elliptical scatter clouds fall outside the region. This indicates that $\mathcal{U}_d$ PDFs can suitably model the entire multitemporal multipolarization data set and are good fits to the data classes resulting in improved segmentation results. The observed elliptical scatter for each class is caused by natural variation and estimator inaccuracy for the finite/small sample sizes being measured.

A mask is applied to mask out mountains and isolate the glacier pixels for classification. The segmentation algorithm was working with 2 × 2 covariance matrix data. Unsupervised contextual non-Gaussian segmentation was then performed using the $\mathcal{U}$-MRF classifier on the terrain corrected dual polarization data set. We fix the number of clusters to 3 for the segmentation. Fig. 7 shows the segmentation results for three SAR images as candidates from each year of the study period. In Fig. 7, bottom figures depict class histograms and fitted model PDFs of the entity trace($\mathbf{\Sigma}^{-1}\mathbf{C}$) for all classes produced by the $\mathcal{U}$-MRF classifier and give a visualization of the goodness-of-fit of the

models. In all cases, the model fit of the class histograms is good. Since the three surface types (GI, SI, and firn) have a distinct backscatter characteristics, they can be reliably discriminated in the segmented images. The firn line, i.e., the boundary between SI and firn is detected in all segmentations. The boundary between SI and GI is also detected. The segmentation results are now validated using in-situ observations. The three GPR ground truth lines acquired in 2005, shown in Fig. 6, are used to label the segmented images into glacier facies and to validate the classification results. The validation is only performed on scenes acquired in spring 2005 that are within a few weeks of the GPR data. Table I reports the overall classification accuracies and omission errors of the glacier zones for the 2005 images. The classification accuracies for the scenes indicate overall accuracies higher than 80% for all cases. We did not find any obvious preference among different configurations because the geometric and radiometric terrain corrections should suppress the effects of both SAR geometry and surface topography on the covariance matrix data sets.

TABLE II
CLASSIFICATION ACCURACIES FOR THE CLASSIFICATION RESULTS FOR THE 2005 IMAGES, INCLUDING OVERALL ACCURACY (OA) AND OMISSION ERROR (OE) FOR THE THREE GLACIER ZONES.

Image	OA %	OE%		
		GI	SI	Firn
20050202IS2ascVV/VH	88.3	18.4	1.5	8.0
20050309IS2ascVV/VH	87.1	19.3	1.8	11.0
20050411IS7desVV/VH	81.1	18.9	4.3	37.7
20050413IS2ascVV/VH	88.3	17.5	1.3	10.3
20050414IS6ascVV/VH	94.7	1.3	4.8	16.0
20050415IS4ascVV/VH	95.3	1.6	5.9	11.3
20050417IS6desVV/VH	88.0	19.6	0.8	7.3
20050417IS7ascVV/VH	87.4	20.8	1.0	6.7
20050418IS4ascHH/HV	87.9	18.5	0.8	10.30
20050419IS3desHH/HV	86.4	23.5	0.0	6.0
20050421IS1desHH/HV	85.9	24.0	0.0	7.3
20050427IS7desVV/VH	85.7	24.3	0.0	7.7
20050428IS2desVV/VH	86.7	21.3	0.5	9.7
20050428IS3ascVV/VH	87.8	17.8	4.1	8.7
20050429IS1ascVV/VH	87.2	18.1	1.0	14.7
20050429IS4desVV/VH	84.8	26.1	0.0	7.3
20050430IS6ascHH/HV	86.3	23.5	0.0	6.7
20050501IS2desVV/VH	86.4	22.5	0.0	8.7
20050501IS4ascVV/VH	96.2	1.3	4.1	9.7
20050502IS2ascVV/VH	81.9	1.4	6.7	11.0
20050503IS6desHH/HV	95.5	4.2	3.3	6.7
20050505IS3desVV/VH	84.6	25.8	0.0	9.0
20050517IS2desVV/VH	86.5	21.7	0.0	10.3

Next, the images that have been taken on the same day with different geometries are chosen as pairs for the consistency investigation of the classification results. Table III is a list of the total variation of firn line for given pairs and is an indicator of variability of this boundary in terms of percentage of the glacier mask (PGM), the total change area error (TCAE), and equivalent linear displacement (ELD) along the glacier. Among these three indicators, the ELD may be a very robust indicator, because the other two depend on the size of the glacier and the accuracy of its mask. An average ELD error of 128 m is obtained between the pairs which is for worst case variation between different configurations. This variation may include the effect of different collection geometries, the segmentation algorithm, and other processing errors. Similar geometries and the segmentation itself should have much reduced variability. Basically, if we have a collection of a time series using data acquired from similar geometries (i.e., an interferometric pairs), then we could anticipate reduced variation and better change detection ability. In such cases, we may not need to perform radiometric terrain correction for change detection.

TABLE III
CONSISTENCY CHARACTERIZATION: THE VARIATION OF FIRN/SI BOUNDARY IN TERMS OF PERCENTAGE OF THE GLACIER MASK (PGM), TOTAL CHANGE AREA ERROR (TCAE), AND ELD ERROR FOR SOME PAIRS. IMAGE IDENTITIES ARE GIVEN IN TABLE I.

Image 1	Image 2	PGM	TCAE (m^2)	ELD (m)
I_2	I_3	1.36%	763200	120.74
I_{13}	I_{14}	0.63%	354600	57.70
I_{21}	I_{22}	1.81%	1017000	179.52
I_{24}	I_{25}	1.55%	869400	153.20

After consistency characterization, the classified images are compared and analyzed on a pixel-by-pixel based analysis to form a change matrix which describes the mapping of classes between the images. From this matrix we can extract a simple map of change versus no change, but also more detailed information on the nature of the change. We take the average of several yearly classified images of the study period for change detection analysis. Fig. 8 shows the change images of glacier within the periods of study (2004-2005, 2005-2006, and 2004-2006). It illustrates changes in the locations of boundaries between glacier facies. The firn line monitoring is important for glaciologists, thus we concentrate only on the variation of firn area boundary with SI zone in the quantitative analysis. Total variation of the firn line in terms of both PGM and TCAE (firn to SI) and ELD for change detection pairs are estimated to verify whether significant changes occur for the periods. Table IV indicates measure of variations of firn/SI boundary for those periods. The differences between averages of yearly classified images can only be considered significant when compared to that of the classification total variation. By taking the average classification result over each year, the expected variation of 128 m (between scene pairs with differing configurations) will decrease by $\sqrt{N}$ for the mean, where N is the number of scenes used in the averaging. Therefore, we obtain the reduced variation in the mean of 52.24 m, 26.72 m, and 47.58 m for the years 2004, 2005, and 2006, respectively, to be used when testing significance. The total variation of this boundary found between 2004 and 2005 exceeds the expected classification variation, which indicates significant change for

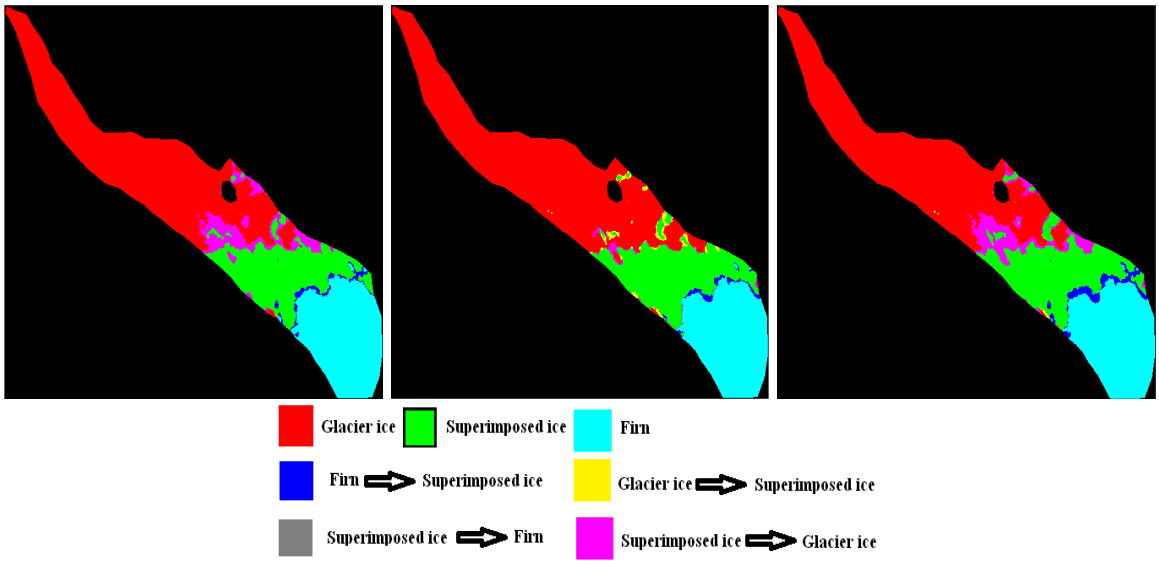

Fig. 8. Change images of Kongsvegen glacier within the periods of 2004-2005 (left), 2005-2006 (middle), and 2004-2006 (right). The changes of firn line for these periods are shown by blue color (movement toward top of the glacier which is bottom right).

this period. The same is found for the periods 2005-2006, 2004-2006. The total movement of the approximately 200 m toward top of the glacier is obtained for the whole period.

TABLE IV
CHANGE DETECTION ANALYSIS: TOTAL ERROR OF FIRN LINE IN TERMS OF PGM, TCAE, AND ELD ERROR FOR THREE PERIODS.

Period	PGM	TCAE (m^2)	ELD (m)
2004-2005	1.36%	764100	127.06
2005-2006	0.69%	358200	107.16
2004-2006	1.78%	980900	203.32

VI. Conclusions and Discussions

This paper addressed glacier change detection from multitemporal multipolarization SAR images. A robust algorithm for firn line monitoring was developed. This suggests that we have a tool for glacier change detection and monitoring that is applicable over the Arctic region on a timescale of a few years. The recent findings may form the basis for more operational monitoring of Arctic areas, which may be even more successful with more capable satellite sensors.

It is noted that when a difference in radar backscattering between multitemporal data is taken as a change indicator, the difference may be due to several factors such as actual land cover change, viewing geometry, surface topography and other external factors (such as meteorological conditions, that are minimized by using radar frequencies and choosing the scenes wisely). These considerations were the main reason for developing a complete workflow for post-classification change detection from time series of polarimetric SAR images, and where we also choose our SAR images to avoid the wet weather conditions.

The algorithm has been tested on dual polarization ENVISAT ASAR images for the period 2004-2006 over the Arctic glacier, Konsvegen, Svalbard. The images are first corrected for terrain effects by thoroughly reducing topographic effects on both geolocation, radiometry and polarization signature, and subsequently stacked into proper time series for further analysis. This is an important step for a meaningful time series analysis.

We showed in [28] that the $\mathcal{K}_d$ distribution can be used to model SAR image texture. However, the analysis shows that this model does not always represent the data well. We then use more flexible model, the multivariate $\mathcal{U}_d$-distribution, for multilook covariance matrix data. The flexibility of this model with respect to $\mathcal{K}_d$ and $\mathcal{G}_d^0$ with an extra texture parameter is evident that covers more of the space of matrix log-cumulant observed in multitemporal dual polarization SAR images. It is expected to yield improved results because of its flexibility to model more varied textures. The matrix log-cumulant diagram was demonstrated for each scene to visualize the capability of the $\mathcal{U}_d$-distribution to model texture observed in multitemporal dual polarization SAR data over this glacier.

We then applied an unsupervised contextual non-Gaussian clustering method, named $\mathcal{U}$-MRF, over terrain corrected SAR scenes. The unsupervised segmentation algorithm together with the DEM-based terrain correction are reliable and robust enough to give consistent change detection results. It should be mentioned that the example glacier was only a very slow moving glacier and the annual change is small. A faster glacier, or other more drastic change examples like deforestation, would likely work much better. Ground truth data are used to label segmented images into the three major classes of glacier facies, i.e., firn, glacier ice (GI), and superimposed ice (SI) and to investigate the classification accuracies.

We then characterized the consistency of the classifica-

tion as the total variation of firn/SI boundary between two no change images to obtain the expected variation just due to processing errors in the processing chain. Finally, we did post-classification change detection analysis based on the classified images on a pixel-by-pixel based analysis. The variations of the boundaries between glacier facies were clearly detected within the period of study. The variation for the two-year period, 2004-2006, exceeds the measured classification variation and thus shows significant change for this period although one year differences were not significant. The fact that we only detect a significant change over two years (with respect to the ELD) is clearly glacier specific. Glaciers in other areas that undergo significant changes may lead to results over a single year.

VII. Acknowledgments

The authors would like to thank Stian Normann Anfinsen for providing MATLAB function for the matrix log-cumulant diagrams, the Northern Research Institute (Norut), Tromsø, Norway, for the Kongsvegen data set and geocoding software, Norwegian Polar Institute for DEM and GPR profiles, the Norwegian Meteorological Institute for the meteorological observations, and the anonymous reviewers for their suggestions that have helped in improving this paper.

References

[1] S. Solomon, D. Qin, M. Manning, Z. Chen, M. Marquis, K. Averyt, M. Tignor, and H. Miller, *IPCC, 2007: Climate Change 2007: The Physical Science Basis. Contribution of Working Group I to the Fourth Assessment Report of the Intergovernmental Panel on Climate Change.* Cambridge, United Kingdom and New York, NY, USA.: Cambridge University Press, 2007.

[2] L. Ulander, "Radiometric slope correction of synthetic aperture radar images," *IEEE Trans. Geosci. Remote Sens.*, vol. 34, no. 5, pp. 1115–1122, Sep. 1996.

[3] D. Small, "Flattening Gamma: radiometric terrain correction for SAR imagery," *IEEE Trans. Geosci. Remote Sens.*, vol. 49, no. 8, pp. 3081–3093, Aug. 2011.

[4] D. Schuler, J. Lee, and T. Ainsworth, "Compensation of terrain azimuthal slope effects in geophysical parameter studies using polarimetric SAR data," *Remote sens. of environment*, vol. 69, no. 2, pp. 139–155, 1999.

[5] J.-S. Lee, D. Schuler, and T. Ainsworth, "Polarimetric SAR data compensation for terrain azimuth slope variation," *IEEE Trans. Geosci. Remote Sens.*, vol. 38, no. 5, pp. 2153–2163, Sep. 2000.

[6] D. K. Atwood, D. Small, and R. Gens, "Improving PolSAR land cover classification with radiometric correction of the coherency matrix," *IEEE J. Sel. Topics Appl. Earth Observ*, vol. 5, no. 3, pp. 848–856, Jun. 2012.

[7] J.-S. Lee, D. L. Schuler, T. L. Ainsworth, E. Krogager, D. Kasilingam, and W.-M. Boerner, "On the estimation of radar polarization orientation shifts induced by terrain slopes," *IEEE Trans. Geosci. Remote Sens.*, vol. 40, no. 1, pp. 30–41, Jan. 2002.

[8] J. S. Lee, D. L. Schuler, R. H. Lang, and K. J. Ranson, "K-distribution for multi-look processed polarimetric SAR imagery," in *IEEE Int. Geosci. Remote Sensing Symp.*, 1994, pp. 2179–2181.

[9] C. Oliver and S. Quegan, *Understanding Synthetic Aperture Radar Images*, 2nd ed. Raleigh, USA: SciTech Publishing, 2004.

[10] A. P. Doulgeris, S. Anfinsen, and T. Eltoft, "Classification with a non-Gaussian model for PolSAR data," *IEEE Trans. Geosci. Remote Sens.*, vol. 46, no. 10, pp. 2999–3009, Oct. 2008.

[11] C. C. Freitas, A. C. Frery, and A. H. Correia, "The polarimetric $\mathcal{G}$ distribution for SAR data analysis," *Environmetrics*, vol. 16, pp. 13–31, 2005.

[12] L. Bombrun, G. Vasile, M. Gay, and F. Totir, "Hierarchal segmentation of polarimetric SAR images using heterogeneous clutter models," *IEEE Trans. Geosci. Remote Sens.*, vol. 49, no. 2, pp. 726–737, Feb. 2011.

[13] S. N. Anfinsen and T. Eltoft, "Application of the matrix-variate Mellin transform to analysis of polarimetric radar images," *IEEE Trans. Geosci. Remote Sens.*, vol. 49, no. 6, pp. 2281–2295, Jun. 2011.

[14] A. P. Doulgeris, V. Akbari, and T. Eltoft, "Automatic PolSAR segmentation with the $\mathcal{U}$-distribution and Markov random fields," in *9th European Conference on Synthetic Aperture Radar (EUSAR)*, Nuremberg, Germany, 23-26 April, 2012, pp. 183–186.

[15] A. P. Dempster, N. M. Laird, and D. B. Bubin, "Maximum likelihood from incomplete data via EM algorithm," *Journal of the Royal Statistical Society. Series B*, vol. 39, no. 1, pp. 1–38, 1977.

[16] J. Besag, "Efficiency of pseudo-likelihood estimation for simple gaussian fields," *Biometrika 64*, vol. 64, no. 3, pp. 616–618, Dec. 1977.

[17] M. König, J. G. Winther, J. Kohler, and F. König, "Two methods for firn-area and mass-balance monitoring of svalbard glaciers with SAR satellite images," *Journal of Glaciology*, vol. 50, no. 168, p. 13 pp., 2004.

[18] J.-S. Lee and E. Pottier, *Polarimetric radar imaging: from basics to applications*, 2nd ed. Boca Raton, USA: CRC Press, Taylor & Francis Group, 2009.

[19] A. Freeman, "SAR calibration: an overview," *IEEE Trans. Geosci. Remote Sens.*, vol. 30, no. 6, pp. 1107–1121, 1992.

[20] C. Wivell, D. Steinwand, G. Kelly, and D. Meyer, "Evaluation of terrain models for the geocoding and terrain correction, of synthetic aperture radar SAR images," *IEEE Trans. Geosci. Remote Sens.*, vol. 30, no. 6, pp. 1137–1144, Nov. 1992.

[21] A. Loew and W. Mauser, "Generation of geometrically and radiometrically terrain corrected SAR image products," *Remote Sensing of Environment*, vol. 106, no. 3, pp. 337–349, Feb. 2007.

[22] J. Curlander and R. McDonough, *Synthetic Aperture Radar-Systems and Signal Processing.* New York: John Wiley & Sons, Inc, 1991., 1991.

[23] J.-S. Lee and T. L. Ainsworth, "The effect of orientation angle compensation on coherency matrix and polarimetric target decompositions," *IEEE Trans. Geosci. Remote Sens.*, vol. 49, no. 1, pp. 53–64, Jan. 2011.

[24] E. Jakeman and P. Pusey, "A model for non-Rayleigh sea echo," *IEEE Trans. Antennas Propag.*, vol. 24, no. 6, pp. 806–814, Nov. 1976.

[25] A. C. Frery, A. H. Correia, and C. d. C. Freitas, "Classifying multifrequency fully polarimetric imagery with multiple sources of statistical evidence and contextual information," *IEEE Trans. Geosci. Remote Sens.*, vol. 45, no. 10, pp. 3098–3109, Oct. 2007.

[26] S. N. Anfinsen, "Statistical analysis of multilook polarimetric radar images with the Mellin transform," Ph.D. dissertation, Faculty of Science and Technology, University of Tromsø, May 2010.

[27] S. N. Anfinsen, A. P. Doulgeris, and T. Eltoft, "Goodness-of-fit tests for multilook polarimetric radar data based on the Mellin transform," *IEEE Trans. Geosci. Remote Sens.*, vol. 49, no. 7, pp. 2764–2781, Jul. 2011.

[28] V. Akbari, A. Doulgeris, G. Moser, T. Eltoft, S. Anfinsen, and S. Serpico, "A textural–contextual model for unsupervised segmentation of multipolarization synthetic aperture radar images," *IEEE Trans. Geosci. Remote Sens.*, vol. 51, no. 4, pp. 2442–2453, Apr. 2013.

[29] G. Celeux, F. Forbes, and N. Peyrand, "EM procedures using mean fieldeld-like approximations for Markov model-based image segmentation," *Pattern Recognition*, vol. 36, no. 1, pp. 131–144, 2003.

[30] R. Engeset, J. Kohler, K. Melvold, and B. Lundén, "Change detection and monitoring of glacier mass balance and facies using ERS SAR winter images over Svalbard," *International Journal of Remote Sensing*, vol. 23, no. 10, pp. 2023–2050, 2002.

[31] S. Evans and B. Smith, "A radio echo equipment for depth sounding in polar ice sheets," *Journal of Physics E: Scientific Instruments*, vol. 2, no. 2, pp. 131–136, 1969.

[32] K. Langley, S.-E. Hamran, K. A. Hogda, R. Storvold, O. Brandt, J. Kohler, and J. O. Hagen, "From glacier facies to SAR backscatter zones via GPR," *IEEE Trans. Geosci. Remote Sens.*, vol. 46, no. 9, pp. 2506–2516, Sep. 2008.

[33] K. Langley, "Glacier subsurface interpretation combining ground penetrating radar and satellite synthetic aperture

radar," Ph.D. dissertation, Faculty of Mathematics and Natural Sciences, University of Oslo, Sep. 2007.

[34] V. Akbari, T. Eltoft, and A. P. Doulgeris, "Non-Gaussian clustering of SAR images for glacier change detection," in *ESA Living Planet Symposium*, 8 pp., 28 June-2 July, 2010.

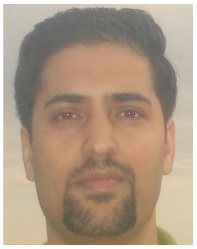

Vahid Akbari (S'10) received the M.Sc. degree in Remote Sensing (*summa cum laude*) from the University of Tehran, Tehran, Iran and the Ph.D. degree in Physics from the University of Tromsø, Tromsø, Norway, in 2009, and 2013, respectively.

His current research interests lies in the field of statistical analysis of polarimetric synthetic aperture radar images and radar interferometry. In particular, his work concerns statistical modeling for segmentation and multitemporal change detection of multi-polarization radar imagery.

Anthony P. Doulgeris (S'06–M'12) received the B.Sc. degree in physics from the Australian National University, Canberra, Australia, in 1988, the M.Sc. degree and the Ph.D. degree in physics from the Department of Physics and Technology, University of Tromsø, Tromsø, Norway, in 2006, and 2011, respectively.

He is continuing his research in applied Earth observation as a postdoctoral research fellow at the Department of Physics and Technology, University of Tromsø, Tromsø, Norway, and is also affiliated with the Barents Remote Sensing School. His research interests focus on investigating remote sensing, pattern recognition and multidimensional statistical modeling, in particular with polarimetric synthetic aperture radar images.

Torbjørn Eltoft (M'92) received the degrees of Cand. Real. (M.Sc.) and Dr. Scient. (Ph.D.) from University of Tromsø, Norway, in 1981 and 1984, respectively. In 1988 he joined the Faculty of Science and Technology, University of Tromsø, where he currently is Head of the Department of Physics and Technology. He is a Professor in electrical engineering, and holds a position as Adjunct Professor at the Northern Research Institute (Norut), Tromsø. His research interests include multi-dimensional signal and image analysis with application in radar remote sensing, statistical models, neural networks, and machine learning. Dr. Eltoft has been Associate Editor of the journal Pattern Recognition for five years. He was the recipient of the year 2000 Outstanding Paper Award in Neural Networks awarded by IEEE Neural Networks Council, and of the Honorable Mention for the 2003 Pattern Recognition Journal Best Paper Award.